A Novel Method for Monitoring Liver Ablation Using Ultrasound Elastography

Hassan Rivaz[a], Ankur Kapoor[b], Ioana Fleming[a], Gregory D Hager[a] and Emad M Boctor[c]

[a]Department of Computer Science, Johns Hopkins University
[b]National Institute of Health
[c]Department of Radiology, Johns Hopkins University

ABSTRACT

Monitoring the ablation process in order to document the adequacy of margins during treatment is of significant importance. Observing that the ablation lesion is harder than normal tissue, it has been proposed to monitor the ablation using ultrasound elastography. Furthermore, it has been reported that the ablated cancer tumor is harder than ablated normal tissue. In this paper we propose an ultrasound elastography technique for visualizing the ablation lesion and the ablated cancerous tumor in Hepatocellular carcinoma (HCC). This work focuses on devising techniques to generate elasticity images which distinguish the ablated cancerous tumor and the ablated normal lesion. We first calculate the displacement field between two ultrasound images acquired before and after some compression. We then use the displacement field to calculate the correlation coefficient between the two images. Parts of the tissue that undergo large deformation give small correlation coefficient due to decorrelation within each window, and parts of the tissue that undergo small deformation give large correlation coefficient. Simulating phantoms with two lesions, a harder tumor inside a hard lesion, using finite element and Field II, we show that this method enables delineating the tumor from the lesion.

1. DESCRIPTION OF PURPOSE

Minimally invasive RF ablation[1] has gained much interest recently since only 10% to 20% of patients with HCC are amenable to traditional therapy of surgical resection of the tumor. In RF ablation, an electrode is placed into the tumor to cauterize it.[1] Monitoring the ablation process in order to document adequacy of margins during treatment is a significant importance. Ultrasonography is the most common modality for both target imaging and for ablation monitoring. However, ultrasonographic appearance of ablated tumors only reveals hyperechoic areas due to microbubbles and outgasing and cannot adequately visualize the margin of tissue coagulation. As a result, the tumor recurrence rate in RF ablation is as high as 34% to 55%.[1, 2]

Ultrasound elastography has emerged as a useful augmentation to conventional ultrasound imaging.[3] In the most common variation of elastography, ultrasound images are captured while the tissue is being compressed, and images are processed to provide a grid of local displacement measurements. These displacement fields are then used to determine the elastic properties of the tissue at each grid location. The grid of calculated elastic properties can be displayed as an image.

Ultrasound elastography has been used to monitor the ablation[4–9] as the ablated lesion is harder than normal tissue. This work is focused on finding the cancerous tumor inside the ablation tumor (the cancerous tumor is believed to be harder than ablation tumor). Previous research has shown that it is possible to delineate a very hard tumor inside a hard lesion[7] using acoustic radiation force impulse imaging.

This paper is focused on freehand palpation elastography, which involves estimating the displacement field of the tissue undergoing slow compression. Most elastography techniques estimate the displacement field using local cross correlation analysis of echoes.[3, 10] These methods are very sensitive and accurate for calculating small displacements. However, elastography is subject to speckle decorrelation caused by various sources such as motion of subresolution scatterers, out-of-plane motion, high compression and complex fluid motions. The prior of tissue deformation continuity can be used to make elastography more robust to signal decorrelation. Previous work on regularized elastography is computationally expensive.[11, 12] Dynamic programming (DP) can be used to speed the optimization procedure,[13] but it only gives integer displacements. Subpixel displacement estimation is possible,[13] but it is computationally expensive if a fine subpixel level is desired. In addition, a fixed regularization weight is applied throughout the image. However, while two ultrasound images may correlate well in most parts, they can have small correlation in specific parts. Four examples of low correlation are: (1) correlation decreases with depth mainly due to a decrease in the ultrasonic signal to noise ratio, (2) correlation is low close to arteries due to complex motion and inside vessels due to blood motion, (3) correlation is extremely low in lesions that contain liquid due to the incoherent fluid motion,[10, 14] and (4) out-of-plane motion of movable structures within the image[14] causes low local correlation.

Having an imaging system that allows the surgeon to distinguish the ablation lesion from the ablated cancerous tumor is of significant importance. In this paper, we first calculate the displacement field between two ultrasound images acquired before and after some compression. We then use the displacement field to calculate the correlation coefficient between the two images. Parts of the tissue that undergo large deformation give small correlation coefficient due to decorrelation within each window, and parts of the tissue that undergo small deformation give large correlation coefficient. To test this hypothesis, we perform simulation studies: using finite element simulation, we first create a model which has two concentric lesions simulating the ablation lesion and the cancerous tumor. We then compress the model and simulate the ultrasound images using Field II.[15] Our results show that the correlation coefficient can show the boundary between the cancerous tumor and ablation lesion.

2. METHODS

2.1 Dynamic Programming (DP)

DP is a discrete efficient optimization technique for causal systems. In DP elastography,[13] a cost function is defined as

$$C(i, d_i) = \min_{d_{i-1}} \{C(i-1, d_{i-1}) + \alpha_a R(d_i, d_{i-1})\} + |I_1(i) - I_2(i + d_i)|, \ i = 2 \cdots m \tag{1}$$

where d_i is the displacement of sample i, $R(d_i, d_{i-1}) = (d_i - d_{i-1})^2$ is an axial regularization term (axial, lateral and out-of-plane directions are respectively z, x and y in Figure 2 (a)), α_a is a weight for the regularization, I_1 and I_2 are corresponding RF-lines of before and after deformation and m is the length of RF-lines. The cost function is minimized at $i = m$ and the d_i values that have minimized the cost function are traced back to $i = 1$, giving the d_i for all samples. We have implemented a 2D DP algorithm similar to[13] to generate integer displacements as a starting point for the next step of our algorithm.

2.2 Analytic Minimization (AM)

We now propose a method that analytically minimizes a regularized cost function and gives the refined displacement field. Only axial displacements will be refined for strain calculation.

Having the integer displacements d_i from DP, it is desired to find Δd_i values such that $d_i + \Delta d_i$ gives the value of the displacement at the sample i for $i = 1 \cdots m$. Such Δd_i values will minimize the following regularized cost function

$$
\begin{aligned}
C \quad (\Delta d_1, \cdots, \Delta d_m) = {}& \Sigma_{i=1}^m \left[I_1(i) - I_2(i + d_i + \Delta d_i) \right]^2 + \\
& \alpha_a(d_i + \Delta d_i - d_{i-1} - \Delta d_{i-1})^2 + \alpha_l(d_i + \Delta d_i - d_i^{p\cdot} - \Delta d_i^{p\cdot})^2
\end{aligned}
\tag{2}
$$

where superscript $p.$ refers to the previous RF-line (adjacent RF-line in the lateral direction) and α_l is a weight for lateral regularization. Substituting $I_2(i + d_i + \Delta d_i)$ with its first order Taylor expansion approximation around d_i, we have

$$
\begin{aligned}
C \quad (\Delta d_1, \cdots, \Delta d_m) = {}& \Sigma_{i=1}^m \left[I_1(i) - I_2(i + d_i) - I_2'(i + d_i)\Delta d_i \right]^2 + \\
& \alpha_a(d_i + \Delta d_i - d_{i-1} - \Delta d_{i-1})^2 + \alpha_l(d_i + \Delta d_i - d_i^{p\cdot} - \Delta d_i^{p\cdot})^2
\end{aligned}
\tag{3}
$$

where I_2' is the derivative of the I_2. The above equation is a quadratic function of Δd_i. Therefore, it can be analytically minimized by setting its derivative with respect to Δd_i to zero and solving for the linear system of equations. Moreover, the coefficient matrix in the linear system is a sparse matrix, which means that solving the system is computationally inexpensive. Details of setting up the system and solving it, as well as making it robust to outliers via iterative reweighted least squares (IRLS) is given in.[9, 16]

2.3 Correlation Coefficient Analysis

In this section, we assume the displacements are known and the goal is to calculate the correlation coefficients. Since the local strain determines the scaling factor between I_1 and I_2, and since scaling reduces the correlation coefficient, we measure the strain indirectly by measuring the correlation coefficient (Figure 1). The displacement d is calculated using DP and AM as discussed in the previous section.

Given the displacement field for the entire image, D, between reference and delayed signals due to compression, we can extract two finite length RF signals, $r_1(t)$ and $r_2(t)$, of length $2W + 1$ centered around sample (i, j), that is

$$
\begin{aligned}
r_1(t) &= I_1(i + w, j) \tag{4} \\
r_2(t) &= I_2(i + D_z(i, j) + w, j + D_x(i, j)) \quad w \in [-W, W] \tag{5}
\end{aligned}
$$

where, D_z and D_x are the axial and lateral components of the displacement field, respectively. Since the displacement estimates are made using speckle data, these two signals are relatively similar. Under ideal situation of no decorrelation due to physical process, the estimate of maximum cross-correlation between these two signal should be unity. However, we observe that these signals differ slightly and the primary cause is due to physical process of variation in compression due to stiffness. The degree of decorrelation is lower in the stiffer regions and increases in less stiffer regions.

We use maximum cross correlation of normalized signals as a measure of this dissimilarity between the two RF data signals, which is defined as

$$
R_{r_1 r_2}(i, j) = \max_{2W+1} \frac{E\left[r_1(t) r_2(t + \tau) \right]}{\| r_1(t) \| \, \| r_2(t) \|}
\tag{6}
$$

where $E\left[.\right]$ is the expectation operator. The resulting image, $R_{r_1 r_2}$, can then be utilized to augment the strain image based on refined displacement map discussed in sections 2.1 and 2.2. Figure 3 shows images obtained from simulated data using a window width of 100 with 90% overlap.
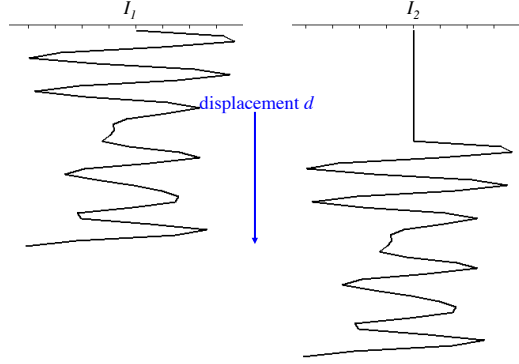
(a) The window is only displaced.
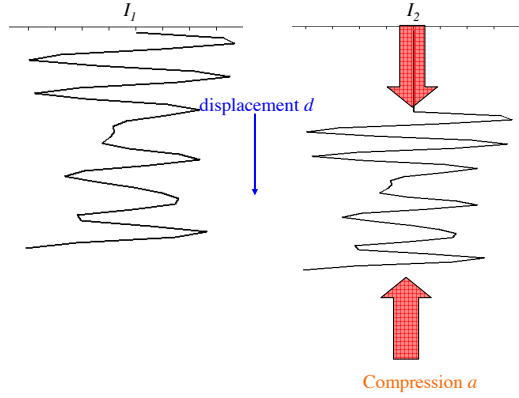
(b) The window is displaced and is scaled.

Figure 1. RF data of a speckle phantom. In (a), the window is only displaced by d. In (b), the window is both displaced and scaled (simulated uniform scaling). The correlation between the two windows in (b) is much smaller than the correlation between them in (a) because of the decorrelation within the window due to the scaling factor.

2.4 Correlation Coefficient Analysis in the Frequency Domain

Another measure of similarity between the two signals over the frequency spectrum is the estimate of magnitude squared coherence, defined as

$$C_{\hat{r}_1 \hat{r}_2}(f) = \frac{|P_{\hat{r}_1 \hat{r}_2}(f)|^2}{P_{\hat{r}_1 \hat{r}_1}(f) P_{\hat{r}_2 \hat{r}_2}(f)} \tag{7}$$

where $P_{\hat{r}_1 \hat{r}_2}(f)$ is the cross power spectrum of the two signals. $P_{\hat{r}_1 \hat{r}_1}(f)$ and $P_{\hat{r}_2 \hat{r}_2}(f)$ are the power spectral densities of the two signals, respectively. We use Welch's method for estimating the power spectral densities. $\hat{r}_1$ and $\hat{r}_2$ are normalized signals, corresponding to r_1 and r_2, respectively. Again, if the corresponding signals are not decorrelated over the entire spectrum, the magnitude squared coherence would be closer to unity.

Using equation 7, we can define an image that is related to the similarity between the two signals over the frequency spectrum as,

$$I_{r_1 r_2}(i, j) = \sum_{f=0}^{F} |C_{\hat{r}_1 \hat{r}_2}(f)|^2 \tag{8}$$

where $F = 2^{\lceil \log_2(W) \rceil} + 1$, is the width of frequency window under consideration. Figure 4 shows the image obtained from stimulated data using a window, W, of 100, with 90% overlap.

3. RESULTS

3.1 Image and Deformation Simulation

Field II[15] and Comsol (Burlington, MA) software are used for ultrasound simulation and for finite element simulation. Many scatterers are distributed in a volume and an ultrasound image is created by convolving all scatterers with the point spread function of the ultrasound and adding the results using superposition. The phantom is then meshed and compressed using finite element simulation, giving the 3D displacement of each node of the mesh. The displacement of each scatterer is then calculated by interpolating the displacement of its neighboring nodes. Scatterers are then moved accordingly and the second (compressed) ultrasound image is generated. The displacement field is then calculated using the AM method and is used to calculate the correlation coefficient.

The parameters of the ultrasound probe are set to mimic commercial 5-10 MHz probes. The probe frequency is 7.27 MHz, the sampling rate is 40 MHz and the fractional bandwidth is 60%. A Hanning window is used for apodization, the single transmit focus is at 22.5 mm, equi-distance receive foci are from 5 mm to 45 mm at each 5 mm, the transmit is sequential, and the number of active elements is 64.

A simulated phantom of size 20 mm x 36 mm x 10 mm is generated as shown in Figure 2. The phantom is made of homogeneous and isotropic material. It contains two circular concentric lesions that are both harder than normal tissue 1×10^5 scatterers with Gaussian scattering strengths[17] are uniformly distributed in the phantom, ensuring more than 10 scatterers[18] exist in a resolution cell.

The mechanical properties of the phantom, required for finite element simulation, are assumed to be isotropic and homogeneous. The elasticity moduli of the background, the ablated normal tissue (at 12 mm diameter) and the ablated cancer tumor (at 6 mm diameter) are respectively 4 KPa, 16 KPa and 30 KPa. A uniform compression in the z direction is applied and the 3D displacement field of phantoms is calculated using ABAQUS. The Poisson's ratio is set to $\nu = 0.49$ in both phantoms to mimic real tissue,[19, 20] which causes the phantoms to deform in x & y directions as a result of the compression in the z direction.

3.2 Correlation Coefficient Results

Using the simulation phantom as described in the previous section, we now apply the correlation techniques to the simulated ultrasound images. Figure 3 shows images obtained from simulated data using a window width of 100 with 90% overlap using Equation 6. We should note that all the correlation values are negated, so that the dark areas correspond to high correlation. This makes the images more comparable with strain images where dark parts correpond to low strain and hard lesions.

Figure 4 shows the image obtained using Equation 8 from stimulated data using a window width of 100, with 90% overlap. This image is also negated, so that the dark part corresponds to high correlation. This makes the images more comparable with strain images where dark parts correpond to low strain and hard lesions.

4. CONCLUSIONS

In this work, we first used the robust DP and AM methods to calculate a displacement map between the two ultrasound images. We then consider windows of the RF data in image 1 and use the displacement map to find their correspondence in image 2. We then calculate the correlation between the two windows. If the windows are large enough, they will suffer from decorrelation due to scaling. We use the decorrelation coefficient to find

(a) Simulation phantom

(b) A scatterer inside the phantom
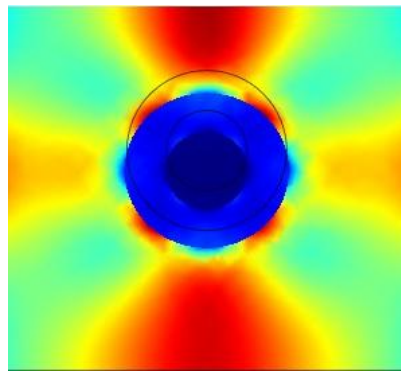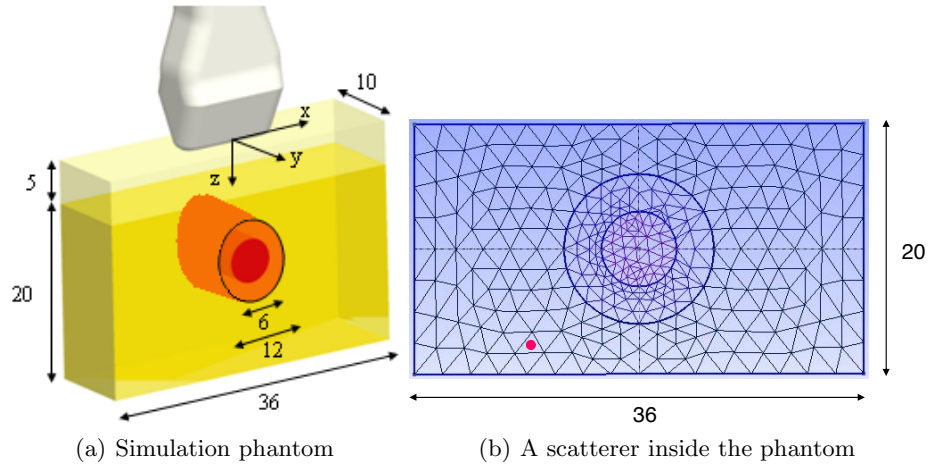
(c) Finite element axial strain
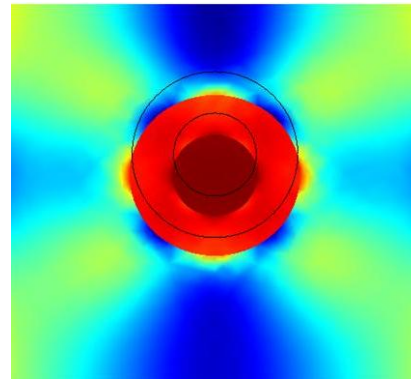
(d) Finite element lateral strain

Figure 2. (a) The simulation phantom with the very hard tumor at the diameter of 6 mm and the hard lesion at the diameter of 12 mm (all the measurements in (a) and (b) are in mm.). The elasticity moduli of the background, the ablated normal tissue (at 12 mm diameter) and the ablated cancer tumor (at 6 mm diameter) are respectively 4 KPa, 16 KPa and 30 KPa. In (b), a scatterer is shown in the bottom left part as a red dot. Its displacement is calculated by interpolating the displacements of its 3 neighboring nodes on the mesh. (c) Ground truth axial strain (FEM results). (d) Ground truth lateral strain (FEM results).

the amount of decorrelation, which leads us to the scaling factor of the RF data. The scaling factor is a good representative of the underlying strain. One disadvantage of this method is that parts of the image that suffer from out-of-plane motion show large decorrelation and might be confused with soft tissue that has undergone large strain. Future work will couple the AM method (which gives the outlier points) with the correlation coefficient technique to identify and eliminate outliers, so that they are not confused with soft tissue.
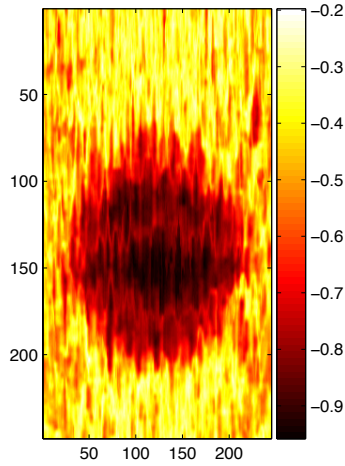
Acknowledgment

Figure 3. The correlation coefficient calculated using Equation 6. All the correlation values are negated so that the dark part corresponds to high correlation. The very dark region in the middle is the simulated ablated tumor, and the surrounding hard area is the ablated normal tissue. The correlation coefficient in the ablated tumor is about 0.95, in the ablated normal tissue is about 0.80 and in the normal surrounding tissue is about 0.4. The strain is not calculated in the right and left boundaries.
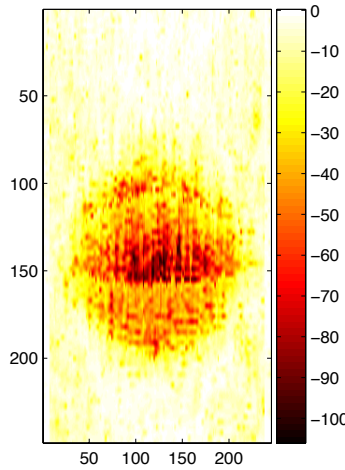

Figure 4. The summation of the magnitude of the squared coherence, as calculated using Equation 8. All the values are negated so that the dark part corresponds to high correlation. The very dark region in the middle is the simulated ablated tumor, and the surrounding hard area is the ablated normal tissue. The brightness values in the ablated tumor is about 100, in the ablated normal tissue is about 40 and in the normal surrounding tissue is about 5. The strain is not calculated in the right and left boundaries.

REFERENCES

[1] Rossi, S., Di-Stasi, M, B. E., and et al., "Percutaneous RF interstitial thermal ablation in the treatment of hepatic cancer," *AJR* **167**, 759–68 (1996).

[2] Solbiati, L., Ierace, T., and et al., "Percutaneous us-guided radio-frequency tissue ablation of liver metastases: treatment and follow-up in 16 patients," *Radiology* **202**, 195–203 (1996).

[3] Ophir, J., Alam, S., Garra, B., Kallel, F., Konofagou, E., Krouskop, T., and Varghese, T., "Elastography," *Annu. Rev. Biomed. Eng.* **213**, 203–233 (Nov. 1999).

[4] Varghese, T., Zagzebski, J., and Lee, F., "Elastography imaging of thermal lesion in the liver following radio frequency ablation: Preliminary results," *Ultrasound Med. Biol.* **28**(11), 1467–1473 (2002).

[5] Varghese, T., Techavipoo1, U., Liu, W., Zagzebski, J., Chen, Q., Frank, G., and Lee Jr, F., "Elastographic measurement of the area and volume of thermal lesions resulting from radiofrequency ablation: Pathologic correlation," *American Journal of Roentgenology* **181**, 701–707 (Sept. 2003).

[6] Kallel, F., Stafford, J., Price, R., Righetti, R., Ophir, J., and Hazle, J., "Elastographic measurement of the area and volume of thermal lesions resulting from radiofrequency ablation: Pathologic correlation," *Ultrasound Med. Biol.* **25**, 641–647 (May 2003).

[7] Fahey, B. J., Hsu, S. J., Wolf, P. D., Nelson, R. C., and Trahey, G. E., "Liver ablation guidance with acoustic radiation force impulse imaging: challenges and opportunities," *Phisics in Medicine and Biology* **51**, 3785 3808 (2006).

[8] Rivaz, H., Fleming, I., Assumpcao, L., Fichtinger, G., Hamper, U., Choti, M., Hager, G., and Boctor, E., "Ablation monitoring with elastography: 2d in-vivo and 3d ex-vivo studies," *Medical Image Computing & Computer Assisted Interventions, MICCAI, New York, NY* , 458–466 (Sept. 2008).

[9] Rivaz, H., Boctor, E., Choti, M., and Hager, G., "Real-time regularized ultrasound elastography," *IEEE Trans Med Imaging* , submitted (2010).

[10] Hall, T., Zhu, Y., and Spalding, C., "In vivo real-time freehand palpation imaging," *Ultrasound Med. Biol.* **29**, 427–435 (Mar 2003).

[11] Pellot-Barakat, C., Frouin, F., Insana, M., and Herment, A., "Ultrasound elastography based on multiscale estimations of regularized displacement fields," *IEEE Trans Med Imaging* **23**, 153–163 (Feb. 2004).

[12] Brusseau, E., Kybic, J., Deprez, J., and Basset, O., "2-D locally regularized tissue strain estimation from radio-frequency ultrasound images: Theoretical developments and results on experimental data," *IEEE Trans Med Imaging* **27**, 145–160 (Feb. 2008).

[13] Rivaz, H., Boctor, E., Foroughi, P., Fichtinger, G., and Hager, G., "Ultrasound elastography: a dynamic programming approach," *IEEE Trans Med Imaging* **27**, 1373–1377 (Oct. 2008).

[14] Lyshchik, A., Higashi, T., Asato, R., and et al., "Thyroid gland tumor diagnosis at US elastography," *Radiology* **237**, 202–211 (Aug. 2005).

[15] Jensen, A., "Field: A program for simulating ultrasound systems," *Medical & Biological Engineering & Computing* **34**, 351–353 (1996).

[16] Rivaz, H., Foroughi, P., Fleming, I., Zellars, R., Boctor, E., and Hager, G., "Tracked regularized ultrasound elastography for targeting breast radiotherapy," *Medical Image Computing & Computer Assisted Interventions, MICCAI, London, UK* , 507–515 (Sept. 2009).

[17] Wagner, R., Smith, S., Sandrik, J., and Lopez, H., "Statistics of Speckle in Ultrasound B-Scans," *IEEE Trans. Sonics and Ultrasonics* **17**(3), 251–268 (1983).

[18] Rivaz, H., Boctor, E., and Fichtinger, G., "Ultrasound speckle detection using low order moments," *IEEE Int. Ultrasonics Symp.* , 2092–2095 (Oct. 2006).

[19] Bertsimas, D. and Tsitsiklis, J., [*Biomechanics: Mechanical Properties of Living Tissues*], Springer-Verlag (1993).

[20] Krouskop, T., Wheeler, T., Kallel, F., Garra, B., and Hall, T., "The elastic moduli of breast and prostate tissues under compression," *Ultras. Imag.* **20**, 260–274 (1998).